



Performance enhancement of an ultrafast graphene photodetector via simultaneous two-mode absorption in a hybrid plasmonic waveguide

HESHAM A. OKDA,^{1,2,*} SHERIF I. RABIA,^{2,3} AND HOSSAM M. H. SHALABY^{1,4}

¹Department of Electronics and Communications Engineering (ECE), Egypt-Japan University of Science and Technology (E-JUST), Alexandria 21934, Egypt

²Department of Engineering Mathematics and Physics, Faculty of Engineering, Alexandria University, Alexandria 21544, Egypt

³Basic and Applied Sciences Institute (BAS), Egypt-Japan University of Science and Technology (E-JUST), Alexandria 21934, Egypt

⁴Electrical Engineering Department, Faculty of Engineering, Alexandria University, Alexandria 21544, Egypt

*Corresponding author: hesham@alexu.edu.eg

Received 25 January 2022; accepted 13 March 2022; posted 17 March 2022; published 6 April 2022

An ultrafast, compact, zero-biased, and complementary metal–oxide semiconductor-compatible graphene photodetector (PD) based on a silicon-on-insulator hybrid plasmonic waveguide (HPWG) is proposed. Lumerical MODE solver is employed to investigate the modal characteristics of TM-polarized modes in the HPWG composing the PD. It is shown that the input light can be completely coupled into the photonic-like and plasmonic-like fundamental TM modes at the PD section. These two modes are exploited together in the photodetection process to enhance the PD performance. A rigorous analysis is performed in order to extract the optoelectronic characteristics of the single-layer graphene (SLG) used in the proposed structure. Lumerical 3D-FDTD solver is then employed to quantify the light interaction of the two aforementioned optical modes with the SLG. With a proper design at a wavelength of 1550 nm, the PD voltage responsivity reaches 2.8 V/W, and the photocurrent responsivity is obtained as 18.5 mA/W, while the corresponding absorption length is kept below 8 μm and the noise equivalent power is limited to 3.7 pW/ $\sqrt{\text{Hz}}$. Moreover, as the PD operates under zero bias, its photoresponse is predominated by the photothermoelectric mechanism, exhibiting a bandwidth that exceeds 180 GHz while avoiding the dark current. © 2022 Optica Publishing Group

<https://doi.org/10.1364/AO.454607>

1. INTRODUCTION

Silicon (Si) photonics is an enabling technology for the integrated optical interconnects operating at the infrared wavelengths beyond 1.1 μm , which allows a dense integration of optical and electronic building blocks on the same chip, based on the mature complementary metal–oxide semiconductor (CMOS) fabrication technology. However, because of the Si transparency at these wavelengths, it cannot be employed effectively to realize photodetectors (PDs) at the receiver end [1–3].

Graphene is a 2D material which is considered a promising candidate for integrated PDs. Single-layer graphene (SLG) has distinctive features, including broadband absorption, ultrahigh carriers' mobilities, CMOS compatibility, and integrability with on-chip photonics platforms such as Si-on-insulator (SOI) [4–6]. Basically, graphene has three mechanisms that may contribute to the overall photoresponse, namely the photovoltaic

(PV) effect, photobolometric (PB) effect, and photothermoelectric (PTE) effect [7,8]. For each specific graphene PD, the dominant mechanism is determined according to the mode of operation (biased or unbiased graphene), device configuration, and design geometry [9].

A wide variety of waveguide-integrated graphene PDs based on PV effect has been reported in literature. For example, in [10], the proposed PD has relied on a metal-doped graphene junction coupled evanescently to an Si waveguide. The electronic band bending at the junction resulted in a built-in electric field that can separate the photogenerated electron–hole pairs under a zero-bias operation. However, the obtained responsivity has been reported to be as small as 15.7 mA/W with an absorption length of 53 μm , and the operation speed is limited by the carriers' mobilities to 20 GHz. With a 1 V bias, the PD responsivity has been reported to reach 0.1 A/W. In addition, the proposed waveguide-integrated PD in [11] has been designed so that the graphene layer has a varying doping level, creating pn

junctions at the contacts. As a result of the asymmetric contact scheme, light is absorbed at only one pn junction, generating a photocurrent with a maximum responsivity of 16 mA/W through a 30 μm PD length, and a bandwidth of 41 GHz under zero bias. On the other hand, in [12], the authors have demonstrated a 50 μm long waveguide-integrated graphene PD operating based on the PB effect under a bias of 1 V. The graphene's resistivity has been changing because of the strong interaction between charge carriers and phonons, resulting in a variation in the flowing current. The reported bandwidth is wider than 76 GHz and the PD responsivity is 1 mA/W.

Several efforts have been made to develop waveguide structures that have the ability to confine light very close to graphene, aiming at enhancing its absorption. One of these structures has been reported in [13], where a SLG is placed on a 100 nm thick Si waveguide and is partially coated by a gold (Au) electrode. Accordingly, the plasmonically enhanced quasi-TE mode is exploited to interact with the graphene, resulting in an improved responsivity of 0.4 A/W under a voltage bias of -0.3 V, along an absorption length of 50 μm . Alternatively, light can be coupled from an Si waveguide to a plasmonic mode confined in a narrow plasmonic gap, as reported in [14–16], which can enhance the PD responsivity up to 0.67 A/W under an 0.5 V bias, with a significant reduction in the absorption length down to 5 μm .

In spite of the enhanced performance of the introduced waveguide-integrated graphene PDs based on PV and PB mechanisms due to the plasmonic effect, they still require operation at an external biasing voltage, which results in an unavoidable noise contribution due to the dark current [17]. Accordingly, the PTE effect is considered of significant importance, as it can be exploited effectively to develop ultrafast PDs operating under zero bias, paving the way for graphene PDs with a vanishing dark current [5]. The PTE mechanism includes the formation of a hot carrier distribution within a very short time interval (<50 fs) as a result of an electron–electron multiple scattering process which occurs in response to an optical excitation. The excited hot carriers cool down over 2–4 ps through a phonon interaction [18,19]. With the presence of a temperature gradient across the SLG, a photovoltage is developed according to the Seebeck effect [20].

Several waveguide-integrated graphene PDs predominated by the PTE mechanism have been reported in literature with a maximum responsivity of 0.36 A/W and a bandwidth of 67 GHz [21–26] although, in these waveguiding structures, the output signal is delivered via two lateral Au contacts. The PTE-induced voltage drop is obtained by integrating the product of the Seebeck coefficient profile and the temperature gradient across the graphene layer. As a result, because of the similar temperature at the contacts, the obtained voltage drop vanishes unless there is a nonzero gradient of the Seebeck coefficient profile across the graphene layer between the two contacts. Accordingly, the common denominator among these structures is the presence of gating voltages in order to electrostatically create areas of different doping levels, and subsequently to generate a varying profile of the Seebeck coefficient across the SLG. Indeed, the demand for such gating voltages leads to more power consumption and raises the design complexity.

In an attempt to get rid of the varying profile of the graphene's Seebeck coefficient, the authors of [27] have recently proposed an alternative design of a graphene PD with two vertical titanium nitride (TiN) electrodes on top of a SLG deposited on an Si rib waveguide. The injected power is partially coupled to a propagating mode in the PD section at a coupling ratio of 0.79 ($\sim 20\%$ coupling loss). The central electrode interacts with the mode field, introducing a plasmonic enhancement to the absorbance of the graphene area below it. Meanwhile, the side electrode is designed to be far enough from the propagating mode, and subsequently almost no absorption occurs below the area of the graphene. Accordingly, the graphene area below the central electrode exhibits higher carrier temperatures than the side area. As a result of this temperature difference at the electrodes, a PTE-induced voltage drop is developed despite the constant profile of the graphene's Seebeck coefficient. Moreover, the use of the TiN as a plasmonic material makes the proposed graphene PD compatible with CMOS technology [28]. The reported bandwidth in that work exceeds 100 GHz, with a nearly flat response over the C-band, although the mode attenuation coefficient has been reported to be 3.67 dB/ μm . This high attenuation coefficient includes both effects of the productive absorption in the graphene and, more significantly, the ohmic loss in the TiN central electrode, which is normally associated with plasmonic-assisted devices. Although the PD responsivity in that work has been reported to be as high as 1.1 A/W, we noticed that the authors have neglected the influence of the TiN-induced ohmic loss on the net graphene's absorption, which we found to significantly reduce the actual PD responsivity, and thus it will be taken into consideration in the present work so that the productive absorption in the SLG is extracted and solely included in the photodetection analysis. Moreover, the authors of [27] have assumed that the SLG is directly deposited on the Si waveguide without an intermediate insulating layer (spacer). However, the existence of such an insulating layer is indispensably required to prevent the injection of SLG's carriers to Si where the SLG is chemically or electrostatically doped to act as a dielectric-like material [29,30].

In this paper, we design a hybrid plasmonic waveguide (HPWG)-integrated graphene PD. The device is based on an SOI strip waveguide in which an SiO_2 spacer is used as an insulating layer between the SLG and the Si waveguide. We first provide a rigorous analysis to help us determine the proper optoelectronic characteristics of the SLG. In addition, we employ Lumerical MODE solver to give an accurate description of the modal behavior of the TM-polarized modes in the presented HPWG-integrated PD. Next, we use Lumerical FDTD solver to carry out the photodetection process in our proposed configuration. We design the PD so that the input power is coupled at nearly zero coupling loss to both photonic-like and plasmonic-like TM-polarized fundamental modes. In addition to the merits offered by the proposed device structure, including bias-free operation, ultra-wide bandwidth (~ 185 GHz), and loss-free input power coupling, our results show that, by properly choosing the thickness of the insulating spacer, the HPWG-integrated graphene PD achieves a reasonable plasmonic enhancement of the graphene absorption, while reducing the associated ohmic loss that is induced by the existence of the TiN central electrode. This leads to a fair compromise between

PD responsivity and noise-equivalent power (NEP) on the one hand and PD absorption length on the other hand.

The remainder of this paper is organized as follows. The structure of the HPWG-integrated graphene PD is described in Section 2. Section 3 is devoted for the theoretical analysis of the proposed device. The obtained results are presented and discussed in Section 4. This is finally followed by the main concluding remarks in Section 5.

2. HPWG-INTEGRATED GRAPHENE PD STRUCTURE AND PRINCIPLE OF OPERATION

The proposed HPWG graphene PD is shown schematically in Fig. 1. It consists of an input SOI strip waveguide, which guides light to the PD section. The PD section is composed of a HPWG with an Si core which is uniformly cladded by SiO₂ to create a spacer with thickness t , to allow a subsequent homogeneous deposition of the SLG on the whole PD area. The spacer insulating layer provides a separation between the Si waveguide and the SLG to inhibit the injection of the graphene's photoexcited carriers into the Si. Besides, the spacer thickness t significantly influences the field distribution of the modes propagating through the waveguide. The SLG is embedded between the SiO₂ spacer and an upper TiN central electrode that introduces a plasmonic confinement of the light close to the graphene area below it, enhancing its effective absorption. At one side of the PD section, another TiN electrode is placed in order to collect the generated photocurrent. At a wavelength $\lambda = 1550\text{nm}$, the refractive indices of the Si and SiO₂ are 3.47 and 1.44, respectively [31]; the TiN refractive index is taken to be $2.54 + 7.84i$ [32].

A. Operation Principle

The main idea of this work is to exploit the unique modal characteristics of the HPWG so that two optical modes can be employed simultaneously in the photodetection process. The input waveguide is launched with the fundamental photonic mode TM₀, which is then totally coupled into two propagating modes at the beginning of the HPWG-integrated graphene PD section, enabling an enhanced excitation of hot carriers with high temperatures in the SLG below the central TiN electrode. Meanwhile, the graphene area below the TiN side electrode exhibits a vanishing interaction with the mode's evanescent field, and thus its carriers maintain the lattice temperature, accounting for an induced voltage difference between the two TiN electrodes, which can be delivered to an external circuit.

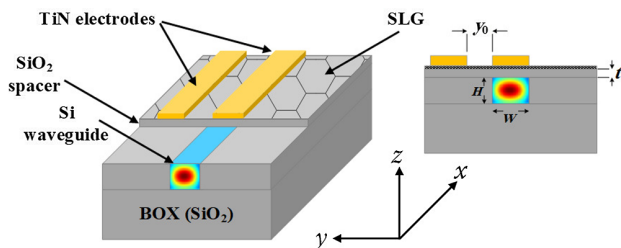


Fig. 1. Structure of proposed HPWG-integrated graphene PD. The coordinate system used in this paper is also shown.

B. Dimensions of Proposed Device

The structural dimensions of the proposed device are determined considering several factors. Namely, the coupling efficiency of the light from the input waveguide to the PD section, strength of the plasmonic confinement of the light close to the graphene, and the overall PD absorption length. We obtained the optimum device dimensions through our initial simulation trials as follows. The waveguide height H and width W are 500 nm each; the spacing between the two electrodes y_0 is set as wide as 150 nm to offer sufficient carriers' temperature gradient; the TiN electrodes have the same waveguide width (500 nm), and their thicknesses are 100 nm each. The TiN electrode's thickness is large to prevent the evanescent field coupling to SPWs at the upper TiN/air interface, and subsequently to reduce the overall plasmonically induced ohmic loss. The spacer thickness t is finally chosen to be 10 nm so that the PD absorption length equals $7.8 \mu\text{m}$.

3. THEORETICAL ANALYSIS

In what follows, we present a full analysis of the proposed HPWG-integrated graphene PD. We start by appropriately modeling the optical and electronic properties of the SLG. Next, we derive proper expressions for the hot carrier's temperature distribution and the PD responsivity.

A. Modeling of SLG

The optoelectronic properties of a SLG are essentially influenced by its chemical potential μ , which can be controlled practically by either electrical gating or chemical doping [33]. The following characteristics of graphene are derived as functions of μ .

Because of the 2D nature of graphene, in which its electrons are confined vertically within the atomic monolayer, the SLG can be modeled as an anisotropic 3D medium of an effective layer thickness $d_g = 0.7 \text{ nm}$. It is worth noticing that the anisotropic treatment of the SLG in the present work is of a high importance to properly describe the SLG interaction with TM modes, which cannot be achieved through the isotropic treatment [34]. In the anisotropic model, the optoelectronic properties of the SLG are identical on the surface plane (i.e., in both x and y directions), in contrast to the normal z direction. Accordingly, while the SLG lacks the out-of-plane optical conductivity $\tilde{\sigma}_\perp$, the surface optical conductivity (in-plane) $\tilde{\sigma}_\parallel$ is expressed, based on Kubo's formula, in a compact form that includes both intra-band and inter-band transitions for $|\mu| \gg K_B T_0$, where K_B is the Boltzmann's constant and T_0 is the lattice temperature, as [29,34]

$$\begin{aligned} \tilde{\sigma}_\parallel = & \sigma_0 \frac{4|\mu|}{\pi \hbar (\Gamma - i\omega)} + \sigma_0 \left\{ 1 + \frac{1}{\pi} \tan^{-1} \left(\frac{\hbar\omega - 2|\mu|}{\hbar\Gamma} \right) \right. \\ & - \frac{1}{\pi} \tan^{-1} \left(\frac{\hbar\omega + 2|\mu|}{\hbar\Gamma} \right) \\ & \left. - \frac{i}{2\pi} \ln \left(\frac{[\hbar\omega + 2|\mu|]^2 + [\hbar\Gamma]^2}{[\hbar\omega - 2|\mu|]^2 + [\hbar\Gamma]^2} \right) \right\}, \end{aligned} \quad (1)$$

where $\tilde{\sigma}_0 = e^2/(4\hbar) \approx 60.85 \mu\text{S}$ is the high-frequency surface optical conductivity of the SLG, e is the electron charge, \hbar is the reduced Planck's constant, ω is the angular frequency of the incident light, and $\hbar\Gamma$ is the effective scattering rate of the charged particles, which has been extracted to be $\sim 59 \text{ meV}$ for a SLG deposited on an SiO_2 substrate [35–37].

The SLG complex volumetric permittivity $\tilde{\epsilon}$ is represented by a diagonal tensor, which can be written as [38]

$$\tilde{\epsilon} = \begin{bmatrix} \tilde{\epsilon}_{xx} = \tilde{\epsilon}_{\parallel} & 0 & 0 \\ 0 & \tilde{\epsilon}_{yy} = \tilde{\epsilon}_{\parallel} & 0 \\ 0 & 0 & \tilde{\epsilon}_{zz} = \tilde{\epsilon}_{\perp} \end{bmatrix}, \quad (2)$$

where $\tilde{\epsilon}_{\parallel}$ is the in-plane conductivity, which is related to $\tilde{\sigma}_{\parallel}$ through:

$$\tilde{\epsilon}_{\parallel} = \epsilon_0 \left(\epsilon_r + \frac{i\tilde{\sigma}_{\parallel}}{\omega\epsilon_0 d_g} \right). \quad (3)$$

Here, the out-of-plane permittivity $\tilde{\epsilon}_{\perp} = \epsilon_0\epsilon_r$, where $\epsilon_r \approx 2.5$ is the relative background permittivity of the graphene.

At the static limit ($\omega \rightarrow 0$), $\tilde{\sigma}$ approaches the surface electrical conductivity σ , which can be approximated by the following relation for $|\mu| \gg K_B T_0$ [35,39]:

$$\sigma \approx e^2/(\pi\hbar) \sqrt{\left(1 + \frac{\mu^2}{\hbar^2\Gamma^2}\right)}. \quad (4)$$

The thermal conductivity is linked to the electrical conductivity through the Wiedemann–Franz law as [40]

$$\kappa = \frac{\pi^2 K_B^2 T_0}{3e^2} \sigma. \quad (5)$$

As shown in Fig. 1, the proposed graphene PD is self-powered (bias-free), consuming zero DC electrical power, and thus its photoresponse is predominated by the PTE mechanism rather than either the PV or PB mechanisms. The overall cooling rate of the excited hot carriers in graphene has been predicted theoretically by Song *et al.* [41] and verified experimentally by Graham *et al.* [42] as

$$\gamma = A \left(\frac{1}{T_0} + B T_0 \right), \quad (6)$$

where

$$A = \frac{3D^2}{4\pi^2 \rho \hbar^3 v_f^4 K_B} \mu^3, \quad B = \frac{6\zeta(3)e^2 K_B^2 v_f^2}{\pi^2 \hbar v_s^2} \frac{1}{\mu^2 \sigma(\mu)}. \quad (7)$$

Here, $D \sim 20 \text{ eV}$ is the graphene's deformation potential, $v_f = 10^6 \text{ m/s}$ is the Fermi velocity of hot carriers, $v_s = 2 \times 10^4 \text{ m/s}$ is the acoustic phonons' velocity, $\rho = 7.6 \times 10^{-7} \text{ kg/m}^2$ is the graphene mass density, and ζ is the Riemann zeta function.

The first term on the right-hand side of Eq. (6) is related to the intrinsic scattering mechanism in graphene, which involves an acoustic phonon emission with a much slower velocity than free electrons. As a consequence of this velocity mismatch, the energy of the emitted acoustic phonons is greatly restricted by the conservation of momentum. Accordingly, the cooling time mediated by that mechanism exceeds 300 ps. On the

other hand, the second term is related to the supercollision (disorder-enhanced) mechanism, which involves a relaxation of the momentum conservation restriction, allowing the emission of high-energy acoustic phonons; subsequently, the associated cooling time is reduced down to a few picoseconds. It has been found that these two mechanisms dominate at low and high temperatures respectively, with a crossover temperature $T^* = \sqrt{1/B}$.

The carrier's cooling length ξ and the electronic heat capacity C can be expressed as [35,39]

$$\xi = \sqrt{\frac{\kappa}{\gamma C}} \quad \text{and} \quad C = \frac{2\pi K_B^2 T_0}{3\hbar^2 v_f^2} \mu, \quad (8)$$

respectively.

In the PTE mechanism, the generated photovoltage is linked to the hot carriers' temperature gradient through Seebeck coefficient, which is given by [39]

$$S = -\frac{\pi^2 K_B^2 T_0}{3e} \frac{1}{\sigma} \frac{d\sigma}{d\mu}. \quad (9)$$

B. Hot Carriers' Temperature Distribution and PD Responsivity

In the case of a SLG exposed to a uniformly distributed optical power along the x axis, the hot carriers' temperature distribution $T_c(y)$ can be obtained by solving the following one-dimensional (1D) heat transport equation [39,40]:

$$\frac{d^2 T_c}{dy^2} - \frac{1}{\xi^2} [T_c(y) - T_0] + \frac{1}{\kappa} P_{\text{abs}}^*(y) = 0, \quad (10)$$

where $P_{\text{abs}}^*(y)$ is the areal density of the optical power absorbed by the SLG and T_c is the carrier temperature.

However, in our proposed structure in Fig. 1, the optical power comes from a waveguide mode propagating along the x axis with a certain attenuation coefficient $\alpha = 10 \log \frac{4\pi K}{\lambda}$ [dB/ μm], where K is the mode's extinction coefficient, due to the absorption in both SLG and TiN central electrode, which means that the areal density of the absorbed power is no longer uniform along the x direction. Since we keep attention focused on the carriers' temperature distribution across the TiN electrodes (along the y direction), we can still employ Eq. (10) after averaging the two-dimensional areal density of the absorbed power $P_{\text{abs}}^*(x, y)$ along the PD absorption length L . Hence, $T_c(y)$ accounts for the average hot carriers' temperature distribution, and the averaged areal density of the absorbed power $P_{\text{abs}}^*(y)$ is given by

$$P_{\text{abs}}^*(y) = \frac{1}{L} \int_{PD} P_{\text{abs}}^*(x, y) dx, \quad (11)$$

where the integration is performed along the PD absorption length L , which is expressed according to the Beer-Lambert law in terms of the mode attenuation coefficient α and the fraction of input power being absorbed $A(L)$ as

$$L = -\frac{1}{\alpha} 10 \log(1 - A(L)). \quad (12)$$

In order to get $P_{\text{abs}}^*(x, y)$, we simply integrate the volumetric density of the absorbed power along the SLG thickness d_g as

$$P_{\text{abs}}^*(x, y) = \frac{1}{2} \omega \Im\{\tilde{\epsilon}_{\parallel}\} \times \int_{\text{SLG}} |E_{g,x}(x, y, z)|^2 + |E_{g,y}(x, y, z)|^2 dz, \tag{13}$$

where the integration is carried out along the effective thickness of the SLG d_g ; $E_{g,x}$ and $E_{g,y}$ are respectively the x and y components of the electric field vector inside the SLG. The integration is performed with high-accuracy mesh settings of the FDTD solver so that we can obtain values of the electric field components at multiple points inside the SLG.

It is worth noticing that, when solving Eq. (10), the boundary conditions $T_c(\pm(y_0 + W/2)) = T_0$ are considered, provided that the separation between the TiN electrodes $|y_0|$ is large enough so that light interaction with SLG is negligible below the side electrode, and subsequently $P_{\text{abs}}^*(|y_0 + W/2|)$ is sufficiently small. Moreover, it is evident from Eq. (13) that the out-of-plane electric field component $E_{g,z}$ does not contribute to the absorption process. This is a result of the anisotropic treatment of the SLG, in which the optical conductivity vanishes in the z -direction, and subsequently $\Im\{\tilde{\epsilon}_{\perp}\} = 0$.

The nonzero temperature gradient across the y axis is responsible for the development of an induced PTE voltage difference across the SLG between the two TiN electrodes according to the Seebeck effect as

$$V_{\text{PTE}} = S(T_c|_{\text{max}} - T_0), \tag{14}$$

where $T_c|_{\text{max}}$ is the carrier temperature at the center of the waveguide (i.e., at $y = 0$). The corresponding photocurrent can be obtained by dividing V_{PTE} by the SLG resistance as

$$I_{\text{ph}} = \frac{\sigma L}{y_0} V_{\text{PTE}}. \tag{15}$$

Throughout this work, our obtained results are all normalized to the input mode power in the PD section. Accordingly, the internal voltage responsivity R_v and current responsivity R_i are directly estimated through Eqs. (14) and (15), respectively. Moreover, the external responsivities can be readily obtained by multiplying R_v and R_i by the power coupling efficiency η between the input photonic mode and the PD mode.

The intrinsic NEP of the PD is determined by calculating the Johnson-Nyquist noise as [27]:

$$\text{NEP} = \frac{\sqrt{4K_B T R_g}}{R_v}, \tag{16}$$

where $R_g = y_0/(\sigma L)$ is the SLG resistance.

4. RESULTS AND DISCUSSION

We start by exploring the modal properties of the HPWG, which allows us to determine the proper PD design. Next, we investigate the optical and electronic characteristics of the SLG, based on the analytical model provided in Section 3.A. After that, the performance of our proposed PD is examined according to the introduced analysis in Section 3.B.

A. Modal Characteristics of HPWGs

Despite the fact that such a HPWG presented in Fig. 1 supports both TM- and TE-polarized modes, only the former can effectively exhibit a plasmonic confinement close to the upper metallic film due to the direction of their principal electric field component that lies tangentially to the film, allowing a strong coupling to surface plasmon waves [43]. Accordingly, we restrict our investigation in the present work to the TM-polarized modes.

Considering an HPWG structure with no spacer (i.e., $t = 0$), we notice that there are two sets of TM-polarized modes: the photonic modes, which are mainly concentrated inside the Si core, and the plasmonic modes that are tightly bound to the TiN–Si interface. In Figs. 2(a) and 2(b), we illustrate the electric field intensity of the fundamental mode TM_0 from each set.

The existence of a nonzero-thickness spacer can be thought of as a perturbation that has been introduced to the structure, which enables evanescent field couplings among the two sets of modes, producing photonic-like as well as plasmonic-like modes. In this context, it is worth noticing that the plasmonic-like modes in a HPWG are typically referred to as hybrid modes [43]. For further clarification, we use Lumerical MODE solver to obtain Fig. 3, which displays the behavior of the fundamental photonic-like mode TM_0^{ph} and the fundamental hybrid mode TM_0^{pl} .

Figure 3(a) depicts the variation of the mode’s effective index N and extinction coefficient K with the spacer thickness t . For TM_0^{ph} , we find that N decreases monotonically with increasing t , indicating that the photonic mode shown in Fig. 2(a) becomes less confined inside the Si core (as its field spreads into the low-index spacer). Meanwhile, K slightly increases with t since the mode field comes in close proximity to the TiN film, which exaggerates the propagation ohmic loss. However, at

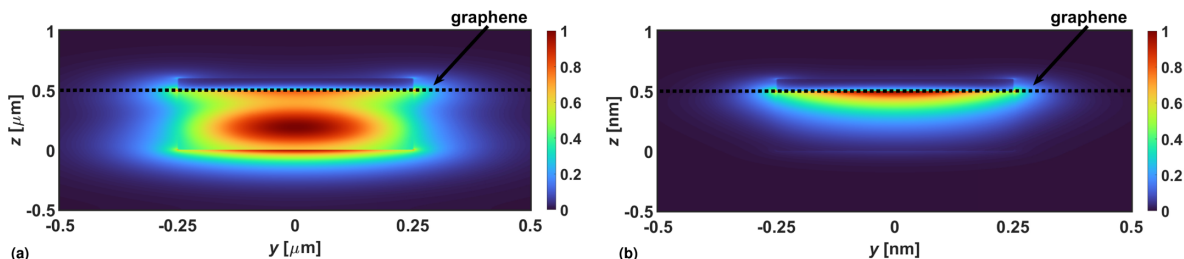


Fig. 2. Electric field intensity of: (a) photonic; (b) plasmonic fundamental modes in a HPWG of a spacer thickness $t = 0$.

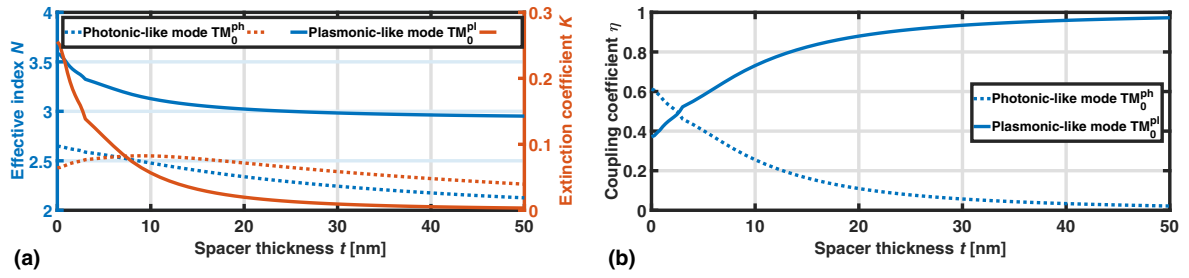


Fig. 3. (a) Effective index and extinction coefficient; (b) power coupling coefficient versus spacer thickness t .

$t = 10$ nm, a turning point comes into view and K starts to decline because the spacer thickness now provides a dielectric separation between the TM_0^{ph} mode field and the film, which in turn reduces the ohmic loss. On the other hand, it is obvious that TM_0^{pl} is more susceptible to the variation of t . Both N and K of that mode significantly drop with increasing t . This is because the optical field of the plasmonic mode shown in Fig. 2(b) is no longer strongly bound to the TiN film, but spreads into the spacer medium (SiO_2), and subsequently its confinement at the film decreases along with its propagation loss. One notices that for $t > 40$ nm, $K \rightarrow 0$, which means that the TM_0^{pl} mode field mostly lies in the low-index spacer with a minimal influence of the TiN film-induced ohmic loss.

In addition, Fig. 3(b) illustrates the power coupling coefficient between the fundamental photonic mode TM_0^{in} that propagates through the input waveguide and either of the modes TM_0^{ph} (η^{in-ph}) or TM_0^{pl} (η^{in-pl}) that propagate through the PD section, versus the spacer thickness t . Interestingly, increasing the spacer thickness t is shown to have a discrepant influence on the coupling coefficients of TM_0^{ph} and TM_0^{pl} with TM_0^{in} . Particularly, η^{in-ph} declines while η^{in-pl} grows, with their sum almost constant at unity. This is because, as t increases, the TM_0^{ph} mode field expands outward from the Si core, decreasing the overlap integral with TM_0^{in} , while the TM_0^{pl} field partially spreads from the vicinity of the TiN film toward the Si core, and thus the overlap integral builds up. Most importantly, since $\eta^{in-ph} + \eta^{in-pl} \approx 1$, this means that almost 100% of the input power of the mode TM_0^{in} is transferred into the modes TM_0^{ph} and TM_0^{pl} for any spacer thickness. The two latter modes contribute together to the PD absorption process, accounting for an effectively zero power coupling loss between the input waveguide and the PD section.

At this point, we design the HPWG with a spacer thickness $t = 10$ nm. Accordingly, the absorption process in the

SLG is mainly contributed by the hybrid mode TM_0^{pl} (with $\eta^{in-pl} = 0.75$) and is assisted by the photonic-like mode TM_0^{ph} (with $\eta^{in-ph} = 0.24$), as obvious from Fig. 3(b). To clarify the optical power confinement of the two aforementioned modes at the SLG, we employ MODE solver to obtain the magnitude of the propagating component of Poynting vector $|P_x(y, z)|$, which is shown in Figs. 4(a) and 4(b) for each mode, respectively. One can see that the modes' radii along the y axis are noticeably smaller than $0.4 \mu\text{m}$ (note that $y = 0.4 \mu\text{m}$ corresponds to the inner edge of the side electrode), which confirms that the temperature of the SLG below that electrode is maintained fixed at T_0 , as pointed out in Section 2.A. The corresponding extinction coefficients K^{ph} and K^{pl} are extracted from Fig. 3(a) and are then substituted into Eq. (12) to obtain the absorption lengths L^{ph} and L^{pl} as $4.7 \mu\text{m}$ and $7.8 \mu\text{m}$, respectively, assuming an absorbed power fraction $A(L) = 0.95$ for each mode. Later, in Section 4.C.2, we perform a similar analysis for different spacer thicknesses and examine the PD performance in each case.

B. Optoelectronic Parameters of SLG

Now, we apply the analytical model introduced in Section 3.A to determine the most suitable chemical potential at which the SLG should be tuned, and thus we can extract its optical and electronic parameters, including the complex permittivity $\tilde{\epsilon}$, cooling rate γ , and Seebeck coefficient S .

Figure 5 illustrates the real and imaginary parts of the surface optical conductivity $\tilde{\sigma}$ as well as the in-plane permittivity $\tilde{\epsilon}_{\parallel}$ at $\lambda = 1550$ nm, based on Eqs. (1) and (2), respectively, versus the chemical potential $|\mu|$. One can notice a significant drop in $\tilde{\sigma}$ at $|\mu| = \hbar\omega/2 \approx 0.4$ eV due to the Pauli blocking effect [44], in which the states of the conduction band are totally occupied, and subsequently the interband transitions [the second term on the right-hand side of Eq. (1)] are inhibited. Furthermore, we find that $\Re\{\tilde{\epsilon}_{\parallel}\}$ tends to have negative values as $|\mu|$ increases towards 0.5 eV, while $\Im\{\tilde{\epsilon}_{\parallel}\}$ settles at zero. Subsequently, the

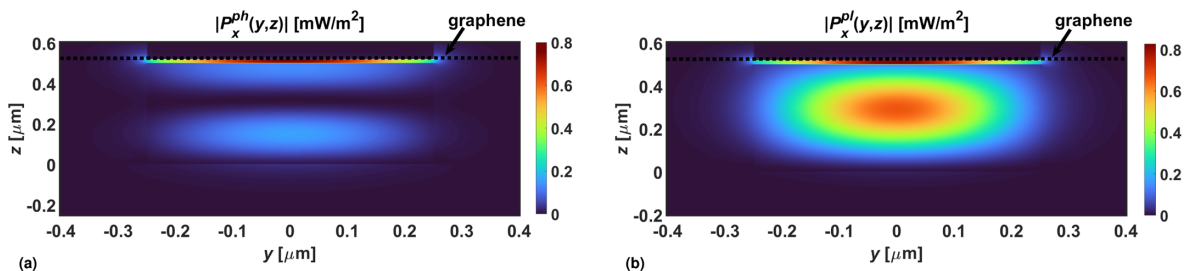


Fig. 4. Magnitude of the propagating component of Poynting vector of (a) photonic-like mode TM_0^{ph} ; (b) hybrid mode TM_0^{pl} .

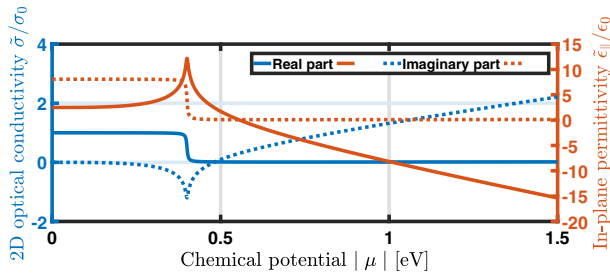


Fig. 5. Real and imaginary parts of surface optical conductivity and in-plane permittivity of SLG versus chemical potential $|\mu|$.

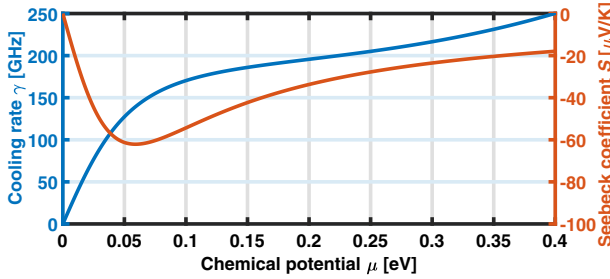


Fig. 6. Hot carriers' cooling rate and Seebeck coefficient of SLG versus chemical potential μ .

Table 1. Optoelectronic Parameters of a SLG Tuned at Chemical Potential $\mu = 0.15$ eV and Wavelength $\lambda = 1550$ nm

$\tilde{\sigma}_{\parallel}$ [mS]	$\tilde{\epsilon}_{\parallel}/\epsilon_0$	σ [mS]	κ [nW/K]	γ [GHz]	ξ [μm]	$ S $ [μV/K]
60.84 + $i0.74$	2.60 + $i8.07$	0.21	1.55	186	0.36	42.3

SLG exhibits a purely imaginary refractive index, indicating that the SLG optical response changes with increase in the chemical potential from being of a dissipative dielectric nature to a perfectly metallic response in which the light is reflected rather than being absorbed. Since the SLG absorption property is principally required to be exploited in our work, we restrict the following results to the chemical potential range $0 < |\mu| < 0.4$ eV.

The PTE-based PD speed is determined according to the cooling rate γ , whereas the magnitude of the PTE induced voltage depends on the Seebeck coefficient $|S|$, as evident from Eq. (14). Accordingly, we make use of Eqs. (6) and (9), respectively, in order to plot both γ as well as S versus the chemical potential μ in Fig. 6. An insight into this figure reveals a trade-off between γ and $|S|$ so that one cannot attain the maximum PD speed simultaneously with the highest responsivity. As a compromise, we suggest tuning the SLG to $\mu = 0.15$ eV to obtain $|S| \sim 42$ $\mu\text{V/K}$, while achieving a PD speed as high as 186 GHz. To summarize, the optoelectronic properties of the SLG tuned at $\mu = 0.15$ eV have been calculated, based on Eqs. (1)–(9), and arranged in Table 1.

C. Evaluating Proposed PD Performance

Here, we come to explore the features of proposed HPWG-integrated graphene PD, considering the aforementioned

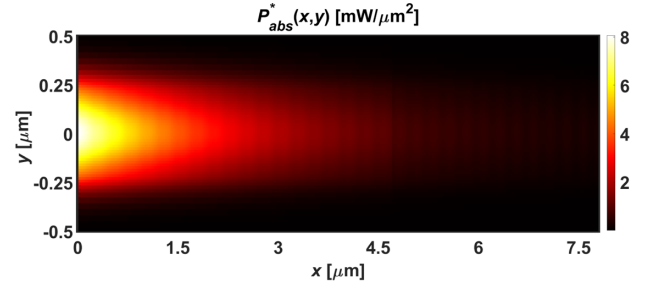


Fig. 7. Areal density of absorbed power in SLG.

design. First, we find the areal density of the total optical power that is exclusively absorbed in the SLG $P_{\text{abs}}^*(x, y)$. Since the two modes TM_0^{ph} and TM_0^{pl} contribute to the absorption process, $P_{\text{abs}}^*(x, y)$ can be expressed as

$$P_{\text{abs}}^*(x, y) = \frac{P_{\text{abs}}^{*\text{ph}}(x, y) + P_{\text{abs}}^{*\text{pl}}(x, y)}{P_{\text{in}}}, \quad (17)$$

where $P_{\text{abs}}^{*\text{ph}}(x, y)$ and $P_{\text{abs}}^{*\text{pl}}(x, y)$ are the areal densities of the absorbed power fraction of each mode, which are carried out separately from Eq. (13). To have the results normalized per unit of the input power, both $P_{\text{abs}}^{*\text{ph}}(x, y)$ and $P_{\text{abs}}^{*\text{pl}}(x, y)$ are divided by the total injected power to the simulation region P_{in} , where $P_{\text{in}} = P^{\text{ph}}/\eta^{\text{in-ph}} = P^{\text{pl}}/\eta^{\text{in-pl}}$; P^{ph} and P^{pl} are the mode power fractions of the two modes TM_0^{ph} and TM_0^{pl} propagating through the PD section, respectively.

Figure 7 illustrates $P_{\text{abs}}^*(x, y)$ as obtained through Eq. (17). The optical power absorption in the SLG is greatly noticed along the first few micrometers of the PD absorption length, showing a fast decay due to the associated power dissipation in the central TiN film along the propagation direction (x axis).

1. Voltage and Current Responsivities

We employ $P_{\text{abs}}^*(x, y)$ in Eq. (11) in order to obtain the averaged distribution of the absorbed power density across the SLG $P_{\text{abs}}^*(y)$. It is worth noticing that, in our case of the two-modes absorption we have $L = \max\{L^{\text{ph}}, L^{\text{pl}}\}$, which is the total absorption length of the PD. We then solve the heat transport equation given by Eq. (10) by using the fifth-order method for solving boundary value problems *bvp5c* provided in Matlab, after properly substituting with $P_{\text{abs}}^*(y)$, along with the extracted parameters of the SLG which are presented in Table 1. Figure 8 depicts $P_{\text{abs}}^*(y)$ and $\Delta T(y) = T_c(y) - T_0$ on the same

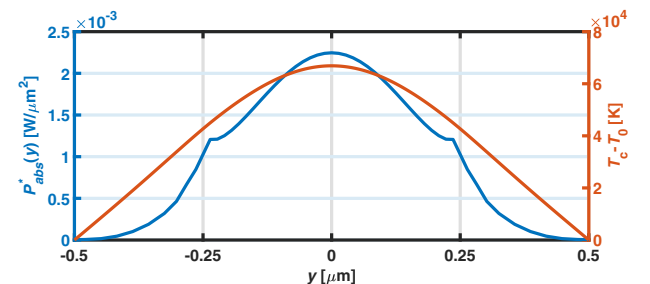


Fig. 8. Averaged areal density of absorbed power (left); hot carriers' temperature distribution across SLG (right).

Table 2. Effect of Changing Spacer Thickness on the Performance of HPWG-Integrated Graphene PD

Spacer Thickness t [nm]	Mode TM_0^{ph}		Mode TM_0^{pl}		R_v [V/W]	R_i [mA/W]	NEP [$\text{pW}/\sqrt{\text{Hz}}$]
	$\eta^{\text{in-ph}}$	L^{ph} [μm]	$\eta^{\text{in-pl}}$	L^{pl} [μm]			
0	0.60	6.0	0.39	1.7	3.8	19.4	2.4
10	0.24	4.7	0.75	7.8	2.8	18.5	3.7
20	0.10	5.6	0.89	21.6	1.0	18.3	17.4
30	0.05	6.9	0.94	44.3	0.5	18.3	51.2

graph, from which $T_c|_{\text{max}} - T_0$ is found to be 6.6×10^4 K. We substitute this value in Eq. (14) to obtain V_{PTE} as 2.8 V. The corresponding photocurrent I_{ph} is also estimated from Eq. (15) to be 18.5 mA.

It is worth noticing that the values obtained for both V_{PTE} and I_{ph} reflect the external voltage and current responsivities, respectively, because of our initial normalization of $P_{\text{abs}}^*(x, y)$ to the total injected power, as seen from Eq. (17).

2. Effect of Spacer Thickness

As evident from Figs. 3(a) and 3(b), both the extinction coefficient K and the coupling coefficient η of the two modes TM_0^{ph} and TM_0^{pl} are sensitive to even slight variations in t . We perform further analysis in order to evaluate the PD performance for various spacer thicknesses. The obtained results are presented in Table 2. One can notice the highest voltage responsivity ($R_v = 3.8$ V/W) for the case of a zero-thickness spacer ($t = 0$). This is due to the strong interaction between both modes TM_0^{ph} and TM_0^{pl} with the SLG in this case. Meanwhile, the corresponding effective absorption length is found to be very short ($L = 6$ μm) because of the excessive power dissipation especially of TM_0^{pl} in the central TiN film. Indeed, this case of a zero-thickness spacer is practically unsuitable because the existence of the spacer is necessary to prevent the injection of graphene's carriers into the Si, as pointed out in Section 2.

As the spacer thickness increases, the role of TM_0^{pl} becomes more significant. Particularly, its coupling with the input mode TM_0^{in} grows. Meanwhile, the influence of the ohmic loss induced by the central TiN film on that mode is significantly reduced, as illustrated in Section 4.A, though as a consequence, the voltage responsivity R_v gradually declines due to the weakened interaction of the modes' fields with the SLG. Furthermore, this comes with increasing the effective absorption length L required to maintain the same absorbed power fraction through the PD (i.e., $A(L) = 0.95$).

The photocurrent responsivity R_i is shown to keep an almost constant value (~ 19 mA/W) despite the reduction in R_v . This is because the latter is compensated by the increase in L , as is obvious from Eq. (15). Moreover, the decline in R_v leads to an exaggerating NEP, according to Eq. (16). Here, we suggest designing our proposed graphene PD with a spacer thickness $t = 10$ nm, which provides a sufficient separation between the SLG's carriers and the Si waveguide [29] while achieving a fair compromise between the PD performance ($R_v = 2.8$ V/W and $\text{NEP} = 3.7$ $\text{pW}/\sqrt{\text{Hz}}$), on the one hand, and its absorption length ($L = 7.8$ μm), on the other hand.

According to the previous discussion, it is clear that the hybrid mode TM_0^{pl} plays a significant role in the photodetection process of the proposed PD. In spite of this, it has not been considered in the analysis reported in the literature [27]. Hence, we argue that our proposed analysis in this work gains the ultimate benefit of the input power by simultaneously employing both modes TM_0^{ph} and TM_0^{pl} in the photodetection process, based on a rigorous model in which the light interaction with the SLG is precisely determined for each mode.

5. CONCLUSION

We have proposed an ultrafast graphene PD that employs a simultaneous absorption of two optical modes propagating through a HPWG in the photodetection process at the telecom wavelength of 1550 nm. The presented PD operates under zero bias, relying on the PTE effect. The modal behavior of the TM-polarized modes in HPWGs has been first investigated using Lumerical MODE solver. It is shown that the HPWG supports two sets of TM modes, which we refer to as photonic-like and plasmonic-like modes. Our results show that the injected power at the input waveguide is entirely coupled with the fundamental mode of each set, which contributes together to photodetection. The anisotropic model of the SLG has been employed to provide the proper optoelectronic characteristics which are fed into Lumerical FDTD solver to find a precious description of the light interaction for each mode with the proposed structure. The PD performance has been estimated for various thicknesses of the insulating spacer that separates the SLG from the Si waveguide. We have finally designed a graphene PD with a spacer thickness of 10 nm so as to achieve a reasonable performance through a short absorption length. The obtained results have come out with a voltage responsivity of 2.8 V/W and a current responsivity of 18.5 mA/W, while the PD absorption length has been found to be as short as 7.8 μm and the NEP is limited to 3.7 $\text{pW}/\sqrt{\text{Hz}}$. A PD speed as high as 185 GHz has also been obtained.

Disclosures. The authors declare no conflicts of interest.

Data availability. Data underlying the results presented in this paper are not publicly available at this time but may be obtained from the authors upon reasonable request.

REFERENCES

1. B. Jalali and S. Fathpour, "Silicon photonics," *J. Lightwave Technol.* **24**, 4600–4615 (2006).
2. P. P. Absil, P. Verheyen, P. De Heyn, M. Pantouvaki, G. Lepage, J. De Coster, and J. Van Campenhout, "Silicon photonics integrated circuits: a manufacturing platform for high density, low power optical I/O's," *Opt. Express* **23**, 9369–9378 (2015).

3. D. Liang, G. Roelkens, R. Baets, and J. E. Bowers, "Hybrid integrated platforms for silicon photonics," *Materials* **3**, 1782–1802 (2010).
4. F. Koppens, T. Mueller, P. Avouris, A. Ferrari, M. Vitiello, and M. Polini, "Photodetectors based on graphene, other two-dimensional materials and hybrid systems," *Nat. Nanotechnol.* **9**, 780–793 (2014).
5. M. Romagnoli, V. Soriano, M. Midrio, F. H. Koppens, C. Huyghebaert, D. Neumaier, P. Galli, W. Templ, A. D'Errico, and A. C. Ferrari, "Graphene-based integrated photonics for next-generation datacom and telecom," *Nat. Rev. Mater.* **3**, 392–414 (2018).
6. N. Youngblood and M. Li, "Integration of 2D materials on a silicon photonics platform for optoelectronics applications," *Nanophotonics* **6**, 1205–1218 (2016).
7. W. H. Wang, H. Y. Nan, Q. Liu, Z. Liang, Z. H. Yu, F. Y. Liu, W. D. Hu, W. Zhang, X. R. Wang, and Z. H. Ni, "Distinct photoresponse in graphene induced by laser irradiation," *Appl. Phys. Lett.* **106**, 021121 (2015).
8. M. Massicotte, G. Soavi, A. Principi, and K.-J. Tielrooij, "Hot carriers in graphene—fundamentals and applications," *Nanoscale* **13**, 8376–8411 (2021).
9. T. J. Echtermeyer, P. Nene, M. Trushin, R. V. Gorbachev, A. L. Eiden, S. Milana, Z. Sun, J. Schliemann, E. Lidorikis, K. S. Novoselov, and A. C. Ferrari, "Photothermoelectric and photoelectric contributions to light detection in metal–graphene–metal photodetectors," *Nano Lett.* **14**, 3733–3742 (2014).
10. X. Gan, R.-J. Shiu, Y. Gao, I. Meric, T. F. Heinz, K. Shepard, J. Hone, S. Assefa, and D. Englund, "Chip-integrated ultrafast graphene photodetector with high responsivity," *Nat. Photonics* **7**, 883–887 (2013).
11. D. Schall, D. Neumaier, M. Mohsin, B. Chmielak, J. Boltzen, C. Porschatis, A. Prinzen, C. Matheisen, W. Kuebart, B. Junginger, W. Templ, A. L. Giesecke, and H. Kurz, "50 GBit/s photodetectors based on wafer-scale graphene for integrated silicon photonic communication systems," *ACS Photon.* **1**, 781–784 (2014).
12. D. Schall, C. Porschatis, M. Otto, and D. Neumaier, "Graphene photodetectors with a bandwidth >76 GHz fabricated in a 6" wafer process line," *J. Phys. D* **50**, 124004 (2017).
13. J. Guo, J. Li, C. Liu, Y. Yin, W. Wang, Z. Ni, Z. Fu, H. Yu, Y. Xu, Y. Shi, Y. Ma, S. Gao, L. Tong, and D. Dai, "High-performance silicon-graphene hybrid plasmonic waveguide photodetectors beyond 1.55 μm ," *Light Sci. Appl.* **9**, 29 (2020).
14. P. Ma, Y. Salamin, B. Baeuerle, A. Josten, W. Heni, A. Emboras, and J. Leuthold, "Plasmonically enhanced graphene photodetector featuring 100 GBit/s data reception, high responsivity, and compact size," *ACS Photon.* **6**, 154–161 (2018).
15. Y. Ding, Z. Cheng, X. Zhu, K. Yvind, J. Dong, M. Galili, H. Hu, N. A. Mortensen, S. Xiao, and L. K. Oxenlowe, "Ultra-compact integrated graphene plasmonic photodetector with bandwidth above 110 GHz," *Nanophotonics* **9**, 317–325 (2020).
16. Z. Ma, K. Kikunaga, H. Wang, S. Sun, R. Amin, R. Maiti, M. H. Tahersima, H. Dalir, M. Miscuglio, and V. J. Sorger, "Compact graphene plasmonic slot photodetector on silicon-on-insulator with high responsivity," *ACS Photon.* **7**, 932–940 (2020).
17. P. C. Eng, S. Song, and B. Ping, "State-of-the-art photodetectors for optoelectronic integration at telecommunication wavelength," *Nanophotonics* **4**, 277–302 (2015).
18. D. Brida, A. Tomadin, C. Manzoni, Y. J. Kim, A. Lombardo, S. Milana, R. R. Nair, K. S. Novoselov, A. C. Ferrari, G. Cerullo, and M. Polini, "Ultrafast collinear scattering and carrier multiplication in graphene," *Nat. Commun.* **4**, 1987 (2013).
19. N. Bonini, M. Lazzeri, N. Marzari, and F. Mauri, "Phonon anharmonicities in graphite and graphene," *Phys. Rev. Lett.* **99**, 176802 (2007).
20. N. M. Gabor, J. C. Song, Q. Ma, N. L. Nair, T. Taychatanapat, K. Watanabe, T. Taniguchi, L. S. Levitov, and P. Jarillo-Herrero, "Hot carrier-assisted intrinsic photoresponse in graphene," *Science* **334**, 648–652 (2011).
21. R.-J. Shiu, Y. Gao, Y. Wang, C. Peng, A. D. Robertson, D. K. Efetov, S. Assefa, F. H. Koppens, J. Hone, and D. Englund, "High-responsivity graphene–boron nitride photodetector and autocorrelator in a silicon photonic integrated circuit," *Nano Lett.* **15**, 7288–7293 (2015).
22. J. Wang, Z. Cheng, Z. Chen, X. Wan, B. Zhu, H. K. Tsang, C. Shu, and J. Xu, "High-responsivity graphene-on-silicon slot waveguide photodetectors," *Nanoscale* **8**, 13206–13211 (2016).
23. S. Schuler, D. Schall, D. Neumaier, L. Dobusch, O. Bethge, B. Schwarz, M. Krall, and T. Mueller, "Controlled generation of a p–n junction in a waveguide integrated graphene photodetector," *Nano Lett.* **16**, 7107–7112 (2016).
24. S. Schuler, D. Schall, D. Neumaier, B. Schwarz, K. Watanabe, T. Taniguchi, and T. Mueller, "Graphene photodetector integrated on a photonic crystal defect waveguide," *ACS Photon.* **5**, 4758–4763 (2018).
25. J. E. Muench, A. Ruocco, M. A. Giambra, V. Miseikis, D. Zhang, J. Wang, H. F. Watson, G. C. Park, S. Akhavan, V. Soriano, M. Midrio, A. Tomadin, C. Coletti, M. Romagnoli, A. C. Ferrari, and I. Goykhman, "Waveguide-integrated, plasmonic enhanced graphene photodetectors," *Nano Lett.* **19**, 7632–7644 (2019).
26. V. Mišėikis, S. Marconi, M. A. Giambra, A. Montanaro, L. Martini, F. Fabbri, S. Pezzini, G. Piccinini, S. Forti, B. Terrés, I. Goykhman, L. Hamidouche, P. Legagneux, V. Soriano, A. C. Ferrari, F. H. L. Koppens, M. Romagnoli, and C. Coletti, "Ultrafast, zero-bias, graphene photodetectors with polymeric gate dielectric on passive photonic waveguides," *ACS Nano* **14**, 11190–11204 (2020).
27. M. AlAloul and M. Rasras, "Plasmon-enhanced graphene photodetector with CMOS-compatible titanium nitride," *J. Opt. Soc. Am. B* **38**, 602–610 (2021).
28. P. Patsalas, N. Kalfagiannis, and S. Kassavetis, "Optical properties and plasmonic performance of titanium nitride," *Materials* **8**, 3128–3154 (2015).
29. S. Ye, Z. Wang, L. Tang, Y. Zhang, R. Lu, and Y. Liu, "Electro-absorption optical modulator using dual-graphene-on-graphene configuration," *Opt. Express* **22**, 26173–26180 (2014).
30. B. H. Nguyen and V. H. Nguyen, "Advances in graphene-based optoelectronics, plasmonics and photonics," *Adv. Nat. Sci.* **7**, 013002 (2016).
31. M. J. Deen and P. K. Basu, *Silicon Photonics: Fundamentals and Devices* (Wiley, 2012), Vol. **44**.
32. J. Goscinia, J. Justice, U. Khan, and B. Corbett, "Study of tin nanodisks with regard to application for heat-assisted magnetic recording," *MRS Adv.* **1**, 317–326 (2016).
33. Q. Bao and K. P. Loh, "Graphene photonics, plasmonics, and broadband optoelectronic devices," *ACS Nano* **6**, 3677–3694 (2012).
34. Y. Meng, S. Ye, Y. Shen, Q. Xiao, X. Fu, R. Lu, Y. Liu, and M. Gong, "Waveguide engineering of graphene optoelectronics—modulators and polarizers," *IEEE Photon. J.* **10**, 6600217 (2018).
35. Y. Lin, Q. Ma, P.-C. Shen, B. Ilyas, Y. Bie, A. Liao, E. Ergeçen, B. Han, N. Mao, X. Zhang, X. Ji, Y. Zhang, J. Yin, S. Huang, M. Dresselhaus, N. Gedik, P. Jarillo-Herrero, X. Ling, J. Kong, and T. Palacios, "Asymmetric hot-carrier thermalization and broadband photoresponse in graphene-2D semiconductor lateral heterojunctions," *Sci. Adv.* **5**, eaav1493 (2019).
36. V. E. Dorgan, M.-H. Bae, and E. Pop, "Mobility and saturation velocity in graphene on SiO₂," *Appl. Phys. Lett.* **97**, 082112 (2010).
37. W. Zhu, V. Perebeinos, M. Freitag, and P. Avouris, "Carrier scattering, mobilities, and electrostatic potential in monolayer, bilayer, and trilayer graphene," *Phys. Rev. B* **80**, 235402 (2009).
38. J.-M. Liu and I.-T. Lin, *Graphene Photonics* (Cambridge University, 2018).
39. J. C. Song, M. S. Rudner, C. M. Marcus, and L. S. Levitov, "Hot carrier transport and photocurrent response in graphene," *Nano Lett.* **11**, 4688–4692 (2011).
40. Q. Ma, N. M. Gabor, T. I. Andersen, N. L. Nair, K. Watanabe, T. Taniguchi, and P. Jarillo-Herrero, "Competing channels for hot-electron cooling in graphene," *Phys. Rev. Lett.* **112**, 247401 (2014).
41. J. C. Song, M. Y. Reizer, and L. S. Levitov, "Disorder-assisted electron-phonon scattering and cooling pathways in graphene," *Phys. Rev. Lett.* **109**, 106602 (2012).
42. M. W. Graham, S.-F. Shi, D. C. Ralph, J. Park, and P. L. McEuen, "Photocurrent measurements of supercollision cooling in graphene," *Nat. Phys.* **9**, 103–108 (2013).
43. H. A. Okda, S. I. Rabia, and H. M. Shalaby, "Sensitivity enhancement of a difference interferometer refractive index sensor based on a silicon-on-insulator hybrid plasmonic waveguide," *J. Opt. Soc. Am. B* **38**, 1405–1415 (2021).
44. A. C. Neto, F. Guinea, N. M. Peres, K. S. Novoselov, and A. K. Geim, "The electronic properties of graphene," *Rev. Mod. Phys.* **81**, 109 (2009).